Journal Pre-proof

Atomistic origin of high-concentration Ce^{3+} in {100}-faceted Cr-substituted CeO_2 nanocrystals

Xiaodong Hao , Akira Yoko , Kazutoshi Inoue , Yang Xu ,
Mitsuhiro Saito , Chunlin Chen , Gimyeong Seong ,
Takaaki Tomai , Seiichi Takami , Alexander L. Shluger ,
Bingshe Xu , Tadafumi Adschiri , Yuichi Ikuhara

Please cite this article as: Xiaodong Hao , Akira Yoko , Kazutoshi Inoue , Yang Xu , Mitsuhiro Saito , Chunlin Chen , Gimyeong Seong , Takaaki Tomai , Seiichi Takami , Alexander L. Shluger , Bingshe Xu , Tadafumi Adschiri , Yuichi Ikuhara , Atomistic origin of high-concentration Ce^{3+} in {100}-faceted Cr- substituted CeO_2 nanocrystals, *Acta Materialia* (2020), doi: https://doi.org/10.1016/j.actamat.2020.11.015

This is a PDF file of an article that has undergone enhancements after acceptance, such as the addition of a cover page and metadata, and formatting for readability, but it is not yet the definitive version of record. This version will undergo additional copyediting, typesetting and review before it is published in its final form, but we are providing this version to give early visibility of the article. Please note that, during the production process, errors may be discovered which could affect the content, and all legal disclaimers that apply to the journal pertain.

Atomistic origin of high-concentration Ce^{3+} in {100}-faceted Cr-substituted CeO$_2$ nanocrystals

Xiaodong Hao[a,b,*], Akira Yoko[b], Kazutoshi Inoue[b], Yang Xu[a], Mitsuhiro Saito[c], Chunlin Chen[b,d], Gimyeong Seong[e], Takaaki Tomai[f], Seiichi Takami[g], Alexander L. Shluger[b,h], Bingshe Xu[a], Tadafumi Adschiri[b,e,f,*], Yuichi Ikuhara[b,c,*]

[a]Materials Institute of Atomic and Molecular Science, Shaanxi University of Science & Technology, Xi'An 710021, China;

[b]WPI-Advanced Institute for Materials Research, Tohoku University, Sendai 980-8577, Japan;

[c]Institute of Engineering Innovation, the University of Tokyo, Tokyo 113-8656, Japan;

[d]Shenyang National Laboratory for Materials Science, Institute of Metal Research, Chinese Academy of Science, Shenyang 110016, China;

[e]New Industry Creation Hatchery Center, Tohoku University, Sendai 980-8579, Japan;

[f]Institute of Multidisciplinary Research for Advanced Materials, Tohoku University, Sendai 980-8577, Japan;

[g]Graduate School of Engineering, Nagoya University, Nagoya 464-8603, Japan;

[h]University College London, Department of Physics & Astronomy, Gower Street, London WC1E 6BT, United Kingdom

*Correspondence should be addressed to: X. Hao (Email: hao.xiaodong@sust.edu.cn) or T. Adschiri (Email: tadafumi.ajiri.b1@tohoku.ac.jp) or Y. Ikuhara (Email: ikuhara@sigma.t.u-tokyo.ac.jp   )

Abstract

Improving the potential of promising CeO_2-based nanocatalysts in practical applications requires an atomic-scale analysis of the effects of active dopants on the distribution of Ce valence states and the formation of oxygen vacancies (V_Os). In this study, a Cr dopant is introduced into the cubic {100}-faceted CeO_2 nanocrystals (NCs) with an average size of 7.8 nm via supercritical water. The Cr dopants substitute Ce sites in the amount of approximately 3 mol%. Based on the aberration-corrected STEM-EELS, the effects of Cr dopant on the distribution of cation valence states in the Cr-doped CeO_2 NCs are investigated layer by layer across the ultrafine Cr-substituted CeO_2 NC perpendicular to the {100} exposed facet. It is found that an increased amount of Ce^{3+} cations is present in Cr-substituted CeO_2 NCs, particularly in the internal atomic layers, compared to the pristine CeO_2 NCs. The atomic-scale analysis of the local structure combined with theoretical calculations demonstrates that Cr dopant reduces the formation energy of V_Os and increases mobility of oxygen atoms for the nano-sized CeO_2. These effects, in principle, result in an improved oxygen storage capacity and provide a fundamental understanding of role of the dopant in the formation and distribution of V_Os in the doped CeO_2 NCs.

Keywords: Cr-substituted CeO_2 nanocrystals; STEM-EELS; The distribution of Ce^{3+} cations; {100} exposing facets; Oxygen storage capacity

1. Introduction

The success in applications of cerium oxides (CeO_2) as environmental catalysts and energy storage-related solid electrolytes stems mainly from its high oxygen storage/release efficiency, the facile formation of oxygen vacancies (V_Os) and the low redox potential for the

2

flexible valence switching of Ce between trivalent and tetravalent states [1-6]. Over the years, researchers have focused on increasing the concentration of V_Os in CeO_2 and improving its reactive efficiency in practical applications. One effective solution is the fabrication of nano-sized CeO_2 with a controllable morphology and narrow size distribution, which have been proven to exhibit the excellent oxygen storage capacity (OSC) and catalytic reactivity [7-12]. With the addition of organic modifiers under homogeneous reaction conditions in supercritical water, monodispersed CeO_2 NCs displaying a cubic shape with {100} facets that are mostly exposed have been fabricated by our group in previous studies [13-17]. The atomic-scale and quantitative analysis show a higher concentration of Ce^{3+} cations, even in the internal atomic layers, in the ultrafine cubic CeO_2 NCs, which lead to the superior OSC performance, even at a low temperatures [17]. Thus, the {100}-facet dominated cubic shape of CeO_2 NCs facilitates the formation of V_Os and promotes high reactivity, particularly when the NC size is reduced below 7 nm, consistent with the previous results [18-20].

Although the controllable synthesis is capable of preparing highly reduced CeO_2 NCs with specific exposed facets and a small size, the limitations of the low reactivity and poor thermal stability of the pristine CeO_2 still persist at higher temperatures [21, 22]. Alternatively, metal ions, such as Zr^{4+}, Ti^{4+}, Y^{3+}, Cu^{2+}, *etc.*, can be introduced into CeO_2 by substitution in the Ce sites with the aim of altering the chemical and physical properties of the host [23-30]. Among all of these metal ions, the Zr dopant has attracted increasing attention mainly because it forms a solid oxide solution of $Ce_{1-x}Zr_xO_2$ ($x \leq 0.5$), and consequently improves the OSC and the practical application in the model system of three-way catalysis [31-34]. Additionally, the valence states of the dopants are known to play a vital role in altering the V_O formation energy, surface acid-base property and reactivity of CeO_2, particularly for dopants with lower valence states than the host cation [35]. In this regard, Singh *et al.* reported a promising system of Cr-doped CeO_2 nanoparticles, which contained a surprisingly high Cr dopant

3

amount of 33% exhibiting flexible-valence states of hexavalent and tetravalent, resulting in a higher OSC performance and enhanced catalytic reactivity of oxygen evolution and hydrogen generation [36, 37]. Recently, highly Cr-substituted CeO_2 NCs was also fabricated using a non-equilibrium supercritical hydrothermal process [38]. Furthermore, Cr-doped CeO_2 nanostructures with a small amount (less than 10%) and a low valence state of Cr^{3+}, other than Cr^{6+} with high toxicity, are also investigated and exhibit high reactivity in diverse processes, such as soot combustion, photocatalytic CO_2 reduction, and electrocatalytic N_2 fixation to NH_3 [39-41]. The incorporation of dopant ions into the lattice of CeO_2 could potentially produce more V_Os, and hence modify its reduction activity, oxygen migration and catalytic properties. Nevertheless, the effect of the Cr dopant on the lattice structure and the distribution of Ce^{3+} cations (or V_Os) inside the CeO_2 NCs, particularly with the size less than 10 nm, still remains poorly understood at the atomic scale.

The synthesis of Cr-substituted CeO_2 NCs with {100} facets that are mostly exposed and display an average size of 7.8 nm has been achieved using the supercritical water reaction in this study. By means of the state-of-the-art aberration corrected scanning transmission electron microscopy (STEM) and electron energy loss spectroscopy (EELS) techniques, it was demonstrated that the Cr dopants substitute approximately 3% the Ce sites. Moreover, the layer-by-layer analysis was also conducted across an ultrafine Cr-substituted CeO_2 NCs perpendicular to the {100} exposed facet for the analysis of the effect of the dopant on the distribution of Ce valence states. A considerably large amount of Ce^{3+} cations is detected in the Cr-substituted CeO_2 NCs, particularly in the internal atomic layers as the particle size ranges from 8.6 to 7.1 nm, in contrast to our previous results of pristine cubic CeO_2 NCs showing that few Ce^{3+} cations are detected in the internal layers on a similar size scale [17]. Theoretical simulations provide the proof that the Cr dopant decreases the formation energy

4

of V_O and increases the mobility of oxygen atoms, resulting in an increased Ce^{3+} cation concentration and OSC performance.

2. Exprimental Sections

2.1. Synthesis of Cr-substituted CeO₂ NCs.

In this study, Cr-substituted CeO_2 NCs were fabricated in supercritical water [16, 17]. Briefly, an aqueous solution of cerium hydroxide was prepared by mixing cerium (III) nitrate hexahydrate (99.99%, Sigma-Aldrich), chromium trichloride (99%, Sigma-Aldrich), and sodium hydroxide (98%, Sigma-Aldrich) with stirring for at least 6 hours. The loading amount of Cr was 5 mol%. The fresh precursor (2.5 mL) prepared as described above was placed in a pressure-resistant Hastelloy vessel (inner volume, 5 mL) with decanoic acid as the organic surfactant (6:1, molar ratio to Ce atom). The mixture was subsequently heated in the reactor at 400 °C for 60 min (10 min for pristine CeO_2 NCs). The reaction was terminated by submerging the reactor into a water bath at room temperature. Afterwards, the as-synthesized Cr-substituted CeO_2 NCs were collected from the mixture and purified using a freeze drying procedure. In addition, the pristine CeO_2 NCs without the addition of the Cr source was also prepared for comparison.

2.2. Structural characterization of the Cr-doped CeO₂ NCs.

Powder XRD measurements were recorded by collecting the diffraction peaks in the range of 20-150° at 1°/min with a 0.005° step size using Smart Lab (RIGAKU). X-rays were mono-chromated to Cu $K_{\alpha1}$ (1.54059 Å) with a Ge(111) curved crystal mono-chromator. Lattice parameters of samples were calculated based on the Rietveld analysis via RIETAN-FP.[42] Similarly, a standard silicon sample was used to calibrate the accuracy of the XRD machine before the measurement. For electron microscopic images, one drop (~10 μL) of

5

collected colloidal solution of Cr-substituted CeO_2 NCs and the pristine CeO_2 NCs was directly deposited onto the ultrathin carbon film (~2 nm, JEOL Ltd.). TEM images were captured using a JEM 2010F (JEOL Ltd.) with an accelerating voltage of 200 kV. Aberration-corrected HAADF-STEM images and EELS spectra were recorded using a JEM-ARM 200F (Cold FEG) at 200 kV with a probe corrector (CEOS, GmbH) and with the energy spread ΔE ~0.3 eV.

2.3. Oxygen storage capacity of the Cr-substituted CeO_2 NCs.

The catalytic properties of the as-synthesized Cr-substituted CeO_2 NCs were evaluated by measuring the OSC performance using a gas adsorption/desorption apparatus (MicrotracBEL, BELSORP CAT-II). Approximately 50 mg of the powder sample of Cr-substituted CeO_2 NCs were loaded and reduced sufficiently by hydrogen gas (99.999%) at the measurement temperature of 300-500 °C and subsequently introduced to an oxygen pulse (99.999%) with a thermal conductor detector (carrier gas: He, 99.999%). The amount of oxygen stored was evaluated based on the O_2 pulse peak. Meanwhile, the sample of the pristine CeO_2 NCs was also tested for comparison.

2.4. Theoretical calculation of the effect of the Cr dopant on the E_{V_0} of CeO_2 NCs.

Plane-wave basis density functional theory (DFT) calculations were conducted to understand the effects of Cr doping on the CeO_2 structure using the VASP code [43, 44]. The generalized gradient approximation (GGA) proposed by Perdew *et al.*[45] was employed as the exchange correlation energy functional. The DFT+U method introduced by Dudarev *et al.*[46] was used to treat electron localization. The parameter U-J was set to 3.5 eV for Cr3d, 5.0 eV for Ce4f, and 5.5 eV for O2p states, respectively, based on previous studies of Cr_2O_3 [47] and CeO_2 [48]. The valence configurations of the pseudopotentials were $3s^23p^63d^54s^1$ for Cr, $5s^25p^64f^15d^16s^2$ for Ce and $2s^22p^4$ for O. The energy cutoff for the plane-wave basis was

set to 500 eV for all calculations and provided the convergence of the total energy in the unit cell of CeO_2. Defect calculations were carried out using the $2 \times 2 \times 2$ extension (96 atoms) of the CeO_2 unit cell (12 atoms) with a Monkhorst–Pack k-point mesh of $4 \times 4 \times 4$. Atomic positions were relaxed within a cubic cell, and the lattice parameters of perfect CeO_2 and Cr-substituted CeO_2 were obtained using the Murnaghan equation of state [49, 50]. Forces were converged to 0.01 eV/Å in all calculations. The calculated crystallographic structure models were visualized via VESTA code [51].

Nudged elastic band (NEB) calculations were performed to obtain diffusion paths and barrier energies with seven replicas, including five nudged intermediate images. The spring constant linking images was 5.0 eV/Å and the conversion criteria were defined such that the resulting forces, including the spring forces, were less than 0.01 eV/ Å. The energy barrier was obtained by applying the climbing image algorithm [52], which enabled the determination of the saddle point at the transition state.

3. Results and Discussions

3.1. Analysis of the microstructure of Cr-substituted CeO_2 NCs.

Fig.1A shows the TEM image of Cr-substituted CeO_2 NCs synthesized in supercritical water. The cubic-like morphology of CeO_2 NCs remained after the introduction of Cr (5%) compared to the pristine CeO_2 NCs (Fig.1B). The cubic morphology of Cr-substituted CeO_2 NCs was further confirmed by the atomic scale high angle annular dark field (HAADF)-STEM images of Cr-substituted CeO_2 NCs depicted Fig.1C, showing that the {100} facets are mostly exposed, which is also confirmed by the inserted FFT pattern along the <001> projection. The crystal structure of the as-synthesized Cr-substituted CeO_2 NCs is indexed to the fluorite-cubic structure of CeO_2 (Fm-3m, Space group 225), showing four strong

7

diffraction peaks of 111, 200, 220, and 311 by powder X-ray diffraction (XRD) pattern, as shown in the Fig.1D, which is consistent with the corresponding selected area diffraction rings shown in the insert in Fig.1A and B. In addition, no Cr-related oxide phase was observed in the XRD pattern, indicating that the segregation of Cr into any type of chromium oxide during the reactions did not occur. The NC sizes was determined by performing a Rietveld analysis of the XRD pattern and was calculated to be 7.8 nm in average for Cr-substituted CeO_2 NCs, a value that is slightly larger than the pristine CeO_2 NCs (average size, 6.6 nm). A prolonged reaction time in the supercritical water was acquired control the morphology and particle size of Cr-substituted CeO_2, which is usually smaller than the pristine CeO_2 under the same synthetic condition [38]. The difference in particle size is probably attributed to the difference in surface energy similar to the previous study [53].
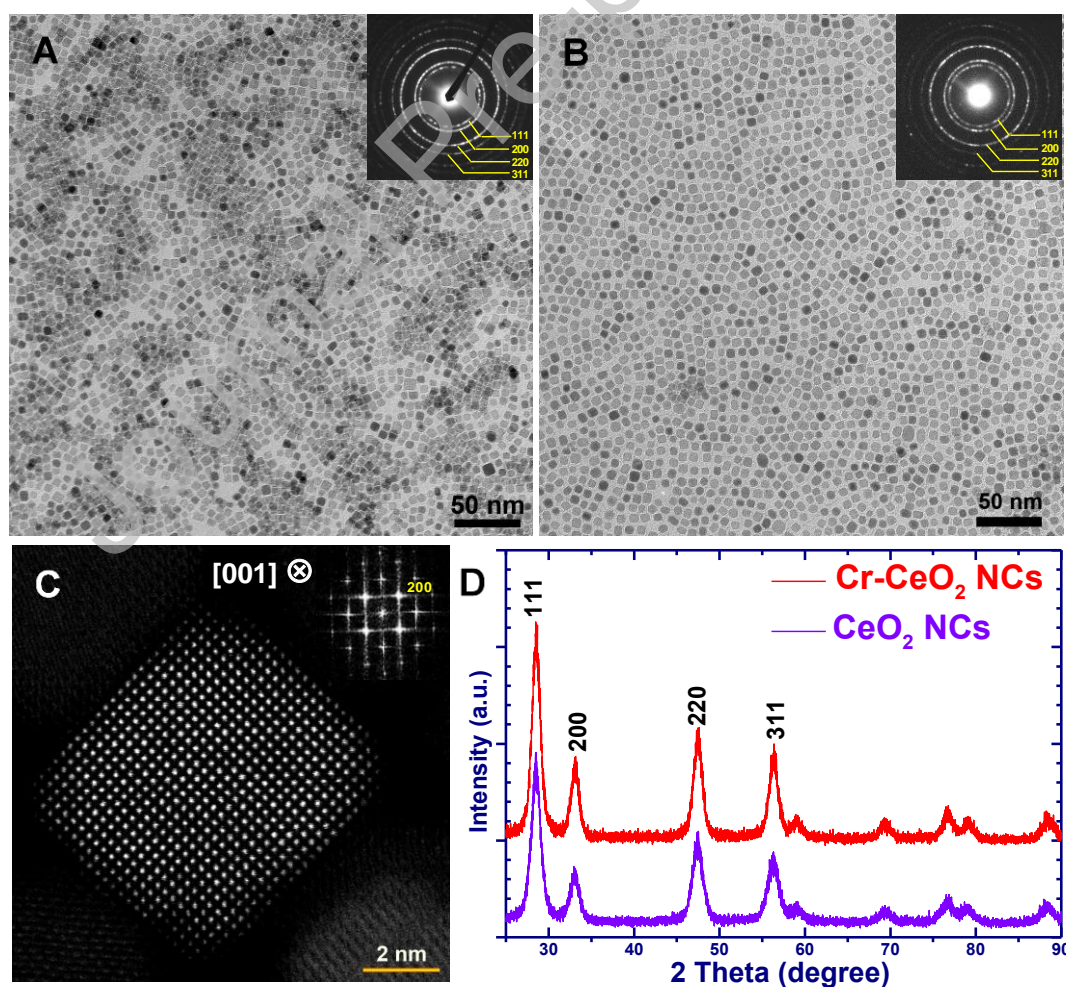
Fig.1. Analysis of the microstructure of Cr-substituted CeO$_2$ NCs. TEM images of (A) as-synthesized Cr-substituted CeO$_2$ NCs and (B) the pristine CeO$_2$ NCs. The insets show the corresponding selected area electron diffraction rings. (C) Atomic-scale HAADF-STEM image of Cr-substituted CeO$_2$ NCs along the <001> projection. The inset is the corresponding FFT pattern. (D) XRD patterns of Cr-substituted CeO$_2$ NCs and the pristine CeO$_2$ NCs.

3.2. The confirmation of the presence of the Cr dopant and its distribution in CeO$_2$ NCs.

STEM-EELS techniques were adopted for the analysis of the amount and distribution of the Cr dopant inside the CeO$_2$ NCs. Fig.2A shows the EELS profiles of the O K edge, Cr L edge acquired from the Cr-substituted CeO$_2$ NCs and pristine CeO$_2$ NCs. The clear "white line" of the Cr L edge at approximately 577.5 eV for Cr-L_3 and 586.0 eV for Cr-L_2 confirmed the presence of the dopant in the as-synthesized Cr-substituted CeO$_2$ NCs. The valence state of the Cr dopant was determined to be Cr^{3+} based on the peak positions of Cr L edge and their energy difference (approximately 8.5 eV), which was attributed to the characteristic of Cr^{3+} in Cr$_2$O$_3$ [54]. In addition, the quantitative analysis revealed a Cr content of approximately 3.0 mol%. Compared to the feeding amount of 5.0 mol%, not all Cr ions participated in the reaction in supercritical water, and the residual Cr ions were washed away during the procedure of product collection. The plausible explanation is that the equilibrium value of Cr dopant in the CeO$_2$ NCs in the particle size of 7.8 nm was approximately 3 mol% under the current reaction conditions. Additionally, the distribution of Cr dopant was examined by the EELS line scan as in Fig.2B. The intensity of Cr signal was multiplied by 4 times for clarification, which are largely consistent with the Ce peaks, as emphasized by the dotted line in the EELS line scan spectrum shown. Based on these results, the introduction of the Cr dopant in a loading amount of 3.0 mol% substituted for the Ce cation sites in cubic NCs.
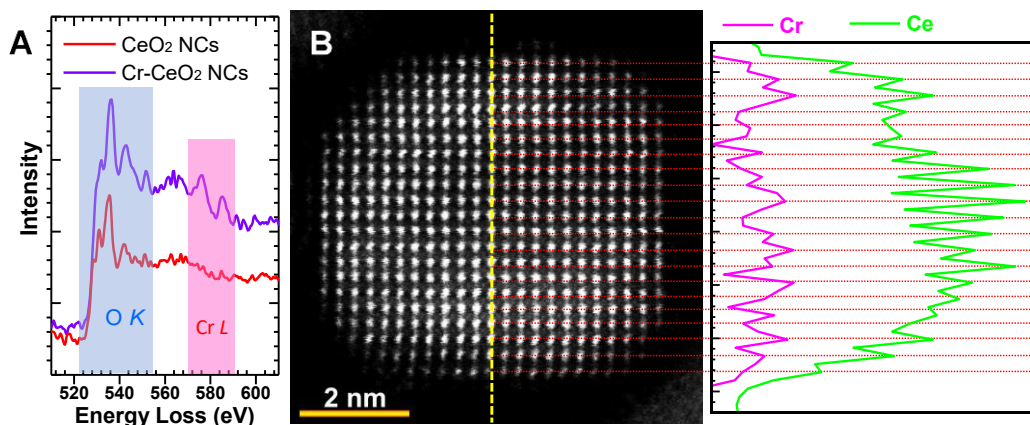
9

Fig.2. The analysis of the Cr dopant and its distribution in the as-synthesized Cr-substituted CeO$_2$ NCs. (A) EELS spectra of the O K edge and Cr L edge for Cr-substituted CeO$_2$ NCs and the pristine CeO$_2$ NCs; (B) HAADF-STEM image of a single Cr-substituted CeO$_2$ NC, and the corresponding elemental EELS line scan profile of Ce and Cr across an atomic layer indicated by the vertical dotted line (yellow).

3.3. Effect of the Cr dopant on the Ce valence states inside the CeO$_2$ NCs.

The STEM-EELS measurements were conducted using the similar method as described in our previous report to study the effect of Cr dopant on the distribution of Ce^{3+} cations in CeO$_2$ NCs [17]. The layer-by-layer EELS spectra across the Cr-substituted CeO$_2$ NC perpendicular to its {100} exposed facet was acquired based on the atomic-resolution HAADF-STEM images, as depicted in Fig.3A and D. For the Ce *M* edge spectra, the featured peaks are clearly shifted to a lower energy loss position mostly at the surface layers in the relatively larger Cr-substituted CeO$_2$ NC (8.6 nm) shown in Fig.3B, in contrast to the relatively smaller NC (5.9 nm) in which the shift occurred at almost all the atomic layers shown in Fig.3E. The shift to a lower energy indicates the existence of reduced Ce cations [17]. Moreover, the plots of the M_5/M_4 ratio calculated using a second derivative method [55] to quantitatively evaluate the Ce valence states are shown in Fig.3C and F. A clear difference in the calculated M_5/M_4 ratio can be seen in these two NCs. For the larger Cr-substituted CeO$_2$ NC (8.6 nm), the calculated M_5/M_4 ratio was similar to the position of Ce^{3+} (purple dot line) in

10

several layers from the surface, while it tended to be located near the position of Ce^{4+} (green dot line) in the center layers. However, for the smaller Cr-substituted CeO_2 NC (5.9 nm), the calculated M_5/M_4 ratio was similar to Ce^{3+} in all the atomic layers from the surface to the center.

Moreover, the EELS measurements and analysis were also conducted in several NCs and the layer-by-layer Ce^{3+} distribution as a function of the size inside Cr-substituted CeO_2 NCs is plotted in Fig.4A.The comparison between the Cr-substituted CeO_2 NCs in the present study and the pristine CeO_2 NCs in the previous study [17] shown in Fig.4B was conducted. A sharp increase in Ce^{3+} was observed in the center layers for the Cr-substituted CeO_2 NCs with sizes ranging from 8.1 to 7.0 nm, which differed from the situation inside the pristine CeO_2 NCs of a similar size. In detail, a Ce^{3+} concentration of 15.6% was detected for the pristine CeO_2 at the size of 8.1 nm, while it increased to 29.4% for the Cr-substituted CeO_2 NCs with a size of 8.1 nm. Moreover, the value increased to 58.4% for the Cr-substituted CeO_2 at the size of 7.1 nm, a value that was twice as larger as the pristine CeO_2 (23.4%) with a size of 7.3 nm. This increase in the Ce^{3+} concentration is attributed to the non-negligible concentration of Ce^{3+} cations detected at the internal atomic layers of Cr-substituted CeO_2 NCs, based on the similar reduction at the surface layers, particular for NCs with a size larger than 7 nm. In addition, a Ce^{3+} concentration of 64.9% was detected for the Cr-substituted CeO_2 with a size of 6.0 nm, and 44.5% for the pristine CeO_2 with a size of 6.1 nm. The NCs size may play a vital role in increasing the Ce^{3+} concentration to a greater extent than the dopant effect, because the surface layers and the internal layers presented a higher Ce^{3+} concentration in both of the Cr-substituted CeO_2 NCs and the pristine CeO_2 when the size was smaller than 6 nm. In total, the Ce^{3+} concentration is much increased in the Cr-substituted CeO_2 NCs compared to the pristine CeO_2 NCs. By combining the results of the layer-by-layer distribution and overall concentration of Ce^{3+} for Cr-substituted CeO_2 NCs, it is feasible to

suggest that the increased Ce^{3+} concentration of was likely caused by the Cr dopant inside the

CeO_2 NCs. The substituted Cr dopants in the Ce lattices, led to the facile formation of Ce^{3+},

particularly in the internal atomic layers of the relatively larger NCs with the size over 7 nm,

in which the cumulative effect of Cr on the valence states of Ce becomes more obvious.
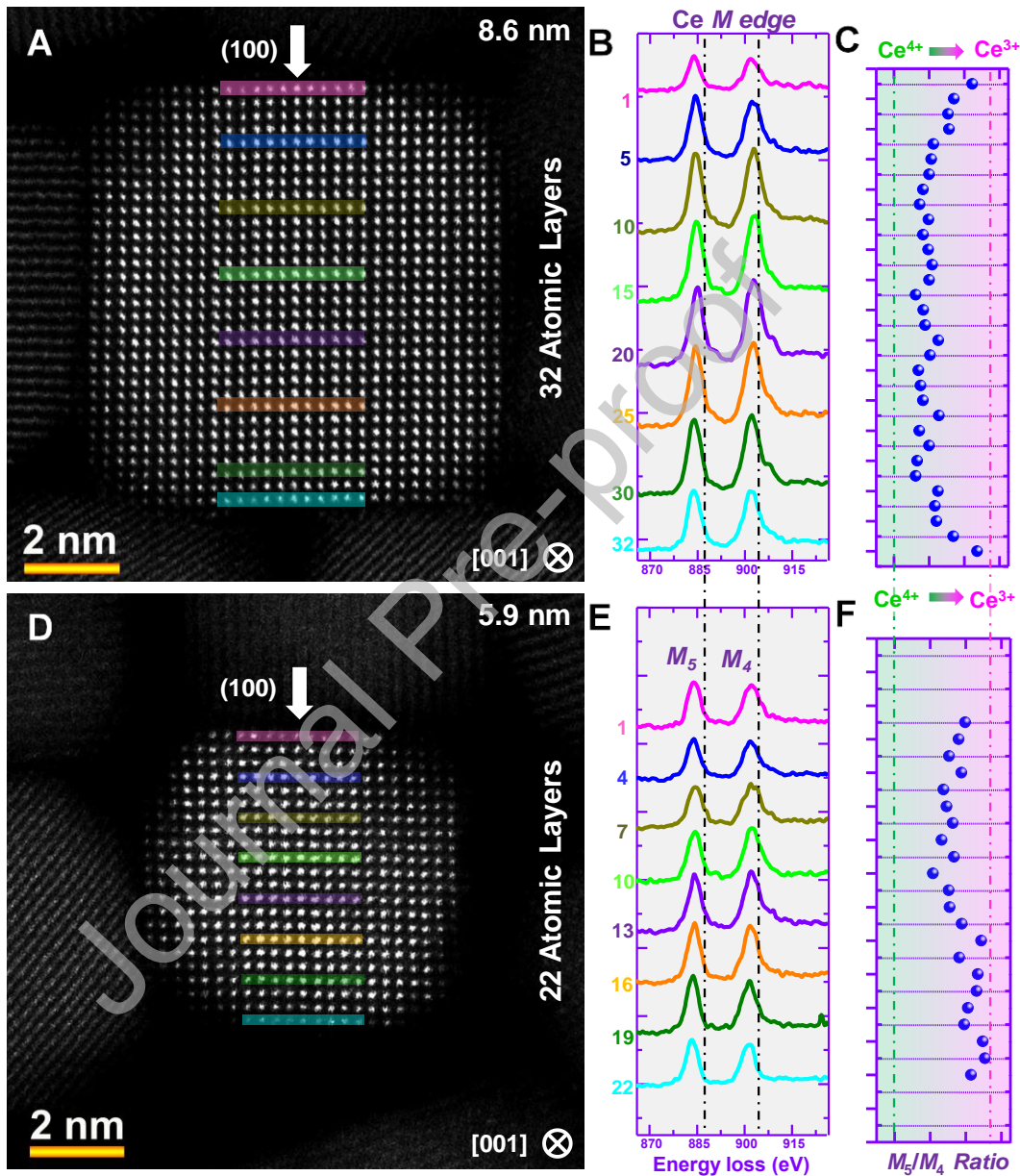

Fig.3. STEM-EELS spectra of Cr-substituted CeO_2 NCs. (A, D) HAADF-STEM images of

Cr-substituted CeO_2 NCs with 32 and 22 atomic layers, respectively; and (B, E) the Ce *M*

edge STEM-EELS spectra acquired layer by layer from the colored boxed area along the

direction indicated by the yellow arrows across the {100} facet. The dotted lines indicate the

M edge position of Ce^{4+}. (C, F) The corresponding M_5/M_4 ratio distribution maps for each layer with the dotted line indicating the reference Ce^{4+} (in green) and Ce^{3+} (in pink).
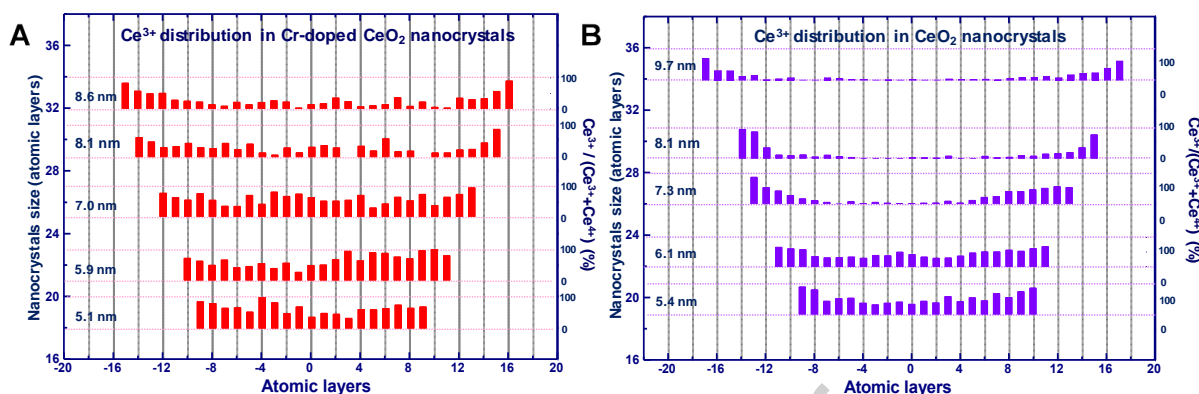

Fig.4. Layer-by-layer Ce^{3+} distribution as a function of the NC size inside (A) the Cr-substituted CeO_2 NCs and (B) the pristine CeO_2 NCs reported previously [17].

3.4. Effect of the Cr dopant on the OSC performance of CeO_2 NCs.

The catalytic properties of such ultrafine and uniform Cr-substituted CeO_2 NCs (with an average size of 7.8 nm) were evaluated by measuring the OSC performance. Meanwhile, the sample of the pristine CeO_2 NCs (average size, 6.6 nm) was also tested in the same procedure. As shown in Fig.5, the sample of Cr-substituted CeO_2 NCs shows OSC values of 242.6, 415.6, and 694.2 μmol-O g^{-1} at 300, 400, and 500 °C, respectively; whereas, for the pristine CeO_2 NCs, the values are 57.8, 188.3 and 353.2 μmol-O g^{-1} at 300, 400, and 500 °C, respectively. Apparently, the OSC performance of Cr-substituted CeO_2 NCs was substantially improved by approximately 4.2-, 1.87-, and 1.67-fold compared with pristine CeO_2 NCs at the test temperatures of 300, 400, and 500 °C, respectively. The OSC of the Cr-substituted CeO_2 NCs may still suffer from the thermal instability when testing at the temperature greater than 400 °C according to the decrease in the performance ratio compared to the pristine NCs. However, our understanding of this process is based on the observation that the Cr-substituted CeO_2 NCs are more reactive than the pristine CeO_2 NCs at 300 °C. For the Cr-substituted CeO_2 NCs with an average size of 7.8 nm, the reactive depth at the surface becomes larger,

13

and/or higher mobility of V_Os allows them to easily diffuse to the surface from the center, where an increased concentration of Ce^{3+} cations were detected as discussed above, ensuring more oxygen atoms participate in the reactions during the process of OSC test than that of the pristine CeO_2 NCs. For understanding of the mechanism of high OSC performance for the Cr-substituted CeO_2 NCs nanocatalysts, it is essential to quantitatively analyze of the distribution of Ce^{3+} cations in {100}-faceted Cr-substituted CeO_2 NCs with the size below 10 nm at an atomic scale. The outstanding performance of Cr-substituted CeO_2 NCs, particularly at the moderate temperature of 300 °C, represents a substantial improvement for the CeO_2-based industrial applications.[14, 56]
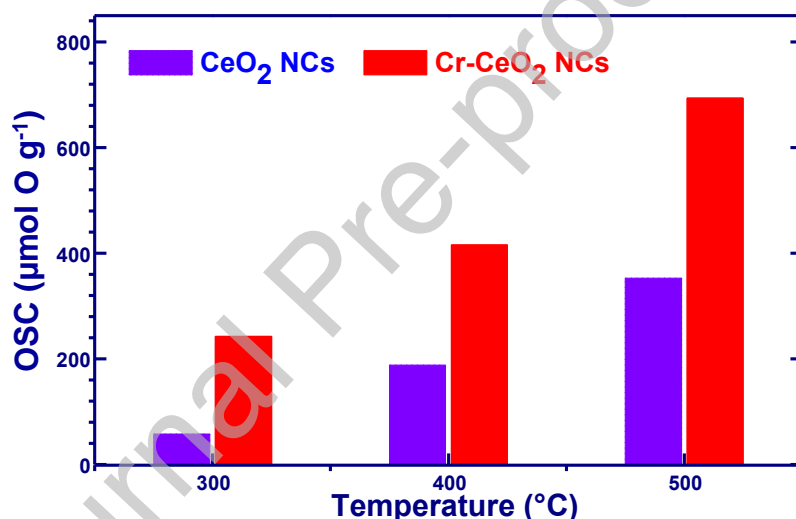

Fig.5. **Oxygen storage capacity (OSC)** of Cr- substituted CeO_2 NCs (average size, 7.8 nm) and the pristine CeO_2 NCs (average size, 6.6 nm) at the test temperatures of 300-500 °C.

3.5. Effect of the Cr dopant on the lattice structure and V_O formation energy of CeO_2 NCs.

The experimental results presented above demonstrate the significant effect of Cr doping and nano-sizing on the concentration of Ce^{3+} in CeO_2 NCs. In particular, the lattice parameters of the as-synthesized Cr-substituted CeO_2 NCs and the pristine CeO_2 NCs are 5.409 and 5.414 Å, respectively, which were calculated from the Rietveld analysis of the

14

XRD spectra. The lattice shrinkage of Cr-substituted CeO_2 NCs can be caused by the smaller ionic radius of Cr^{3+} (0.615 Å) than both Ce^{3+} (1.143 Å) and Ce^{4+} (0.97 Å) ions [57]. The effect of the Cr dopant on the lattice structure is consistent with the previous reports [36, 58]. Moreover, the atomic-scale STEM-EELS analysis provided insights into the distribution of the Cr dopant and its effect on the valence states of Ce cations, and the results adequately explain the improvement in OSC performance. However, the reason why such a small amount of Cr (3 mol%) in CeO_2 NCs induces a much higher Ce^{3+} concentration remains unclear.

To elucidate these issues, density functional theory (DFT) simulations were performed to understand the effects of the Cr dopant on V_Os formation and oxygen mobility. A Ce atom in the 96-atom $2 \times 2 \times 2$ supercell of CeO_2 ($Ce_{32}O_{64}$) was substituted with one Cr atom, which is equivalent to the loading amount of Cr at 3 mol% measured using the STEM-EELS analysis. The formation energy of V_O (E_{V_O}) was calculated as the total energy difference with the chemical potential of an isolated oxygen molecule as a reference using the following equation:

$$E_{V_O} = E^f + \frac{1}{2}\mu(O_2) - E^i \tag{1}$$

where E^i and E^f are the total energies of the supercells of the initial state and the final state with a V_O introduced, respectively. Table 1 summarizes the most stable defect configurations found, E_{V_O} in these configurations as well as effective atomic charges calculated using the Bader population analysis [59]. These configurations are shown in Fig.6. The incorporation of Cr in 3+ charge state can be compensated by the formation of an extra V_O (per two Cr^{3+} ions) or a V_O and a Ce^{3+} ion (see Fig.6C). The oxidation of Cr-substituted CeO_2 NCs, on the other hand, should create Cr^{4+} ions (Fig.6B). Whether the presence of Cr^{3+} ions can facilitate the creation of extra oxygen vacancies (Fig.6D and E) was also considered. Out of the number of

15

possible configurations of V_O, Cr^{3+}, and Ce^{3+} ions, only the most energetically favorable configurations are presented here.

Fig.6A shows the relaxed local structure of a V_O in the pristine CeO_2. Two Ce^{3+} ions are located in the next nearest neighbor (NNN) positions with respect to the V_O, consistent with previous studies of CeO_2 with DFT+U [60, 61]. The Bader charge [59] of the Ce^{3+} ions is equal +2.11 |e| and that of the Ce^{4+} ions is +2.44 |e|. The E_{V_O} in the the pristine CeO_2 is 2.00 eV. As shown in the experimental part, the OSC is substantially improved by Cr doping. Two possible reasons are considered here: one is the contribution of the valence change of Cr to E_{V_O}, and the other factor is the structural effect of Cr doping on E_{V_O}. Only 3 mol% doping improved the OSC by approximately two-fold, suggesting that Cr doping affects the structure of CeO_2 significantly. The results of layer-by-layer EELS analysis indicated a significant increase in the amount of Ce^{3+} by Cr doping, which is more than the mere compensation of Cr^{3+} with V_Os.

Table 1. Structural Data Calculated for Cr-substituted CeO_2 and CeO_2.

Structure	Bader charge, |e|					V_O positions (distance from Cr)	E_{V_O} [eV]	Ce^{3+} positions relative to V_O
	Ce^{3+}	Ce^{4+}	Cr^{3+}	Cr^{4+}	O			
Non-doped CeO_2 with 1 V_O (Fig.6A)	+2.11	+2.44	n/a		-1.28 to -1.20	n/a	2.00	NNN ($2Ce^{3+}$)
Cr^{4+} doped CeO_2 (Fig.6B)	n/a	+2.45	n/a	+2.00	-1.24 to -1.16	No V_O	n/a	n/a
Cr^{3+} doped CeO_2 with 1 V_O (Fig.6C)	+2.15	+2.44	+1.86	n/a	-1.26 to -1.17	O-1 in Fig.6B (2 Å)	0.99	NNN ($1Ce^{3+}$)
Cr^{3+} doped CeO_2 with 2 V_O (Fig.6D)	+2.15	+2.43	+1.85	n/a	-1.27 to -1.20	O-1 in Fig.6B (2 Å)	-	NNN ($3Ce^{3+}$)
						O-2 in Fig.6C (2 Å)	0.65	
Cr^{3+} doped CeO_2 with 3 V_O (Fig.6E)	+2.13	+2.42	+1.85	n/a	-1.37 to -1.20	O-1 in Fig.6B (2 Å)	-	NNN ($5Ce^{3+}$)
						O-2 in Fig.6C (2 Å)	-	
						O-3 in Fig.6D (6 Å)	1.20	

In the first place, the contribution of the valence change of Cr to the OSC enhancement was considered. An oxidative state of Cr-substituted CeO_2 incorporating oxygen atoms is

initially considered and then V_Os are introduced in the structure. Fig.6B shows the structure of the simple substitution of a Ce with a Cr without a V_O, which represents an oxidative state of Cr-substituted CeO_2. In the perfect crystal of CeO_2, Ce atoms are coordinated by eight equivalent oxygen atoms. On the other hand, when a Ce is substituted by a Cr atom, local distortion occurs, and Cr^{4+} is closely coordinated by four oxygen atoms, and other four oxygen atoms move away from Cr. The local structural distortion results in lower E_{V_O} than in the pristine CeO_2. Particularly, E_{V_O} at O sites, which have longer distances from Cr (O-1 in Fig.6B), are 0.99 eV. This structure is more stable than other structures with V_O at different positions. The formation of V_O compensating for Cr^{3+} readily occurs. Fig.6C shows the structure with an oxygen atom (O-1) removed with six coordinated Cr^{3+} local structures forming a Ce^{3+} with an E_{V_O} of 0.99 eV. The Ce^{3+} is located on NNN, similar to the pristine CeO_2.
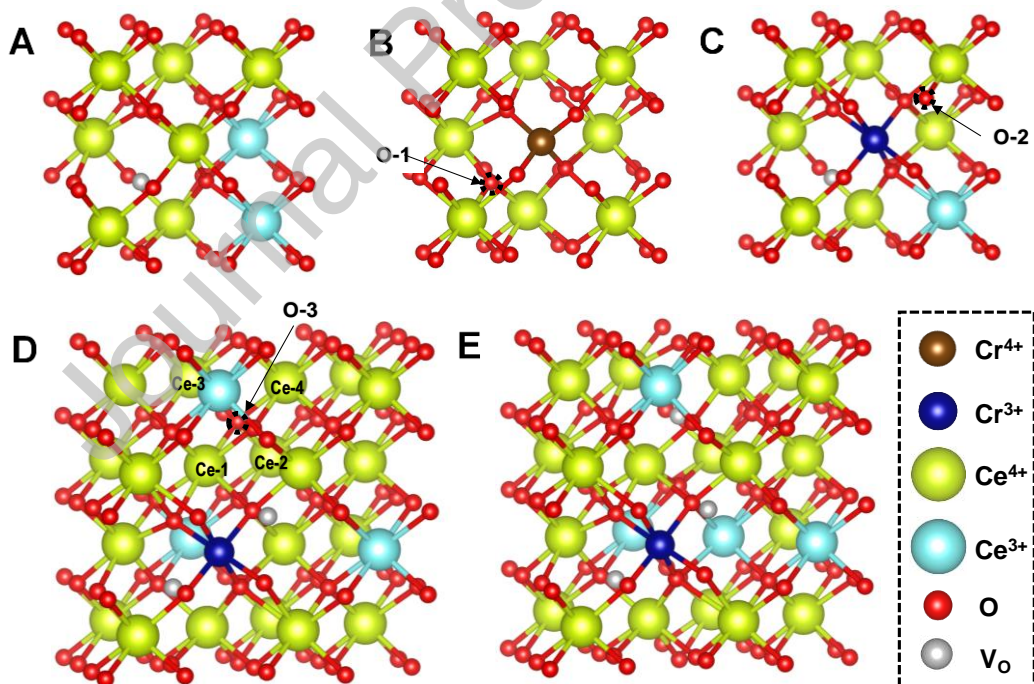

Fig.6. Local structure of (A) pristine CeO_2 with a V_O; (B) Cr^{4+}-substituted CeO_2 without a V_O, where O-1 shows one of the oxygen moving away from Cr after relaxation; (C) Cr^{3+}-substituted CeO_2 with a V_O and Ce^{3+} ion, Cr^{3+} is six-coordinated, and O-2 shows remained non-coordinated oxygen near Cr; (D) a Cr^{3+}, two V_Os, and three Ce^{3+} ions at the NNN of V_O,

where O-3 shows the oxygen site coordinated by four Ce^{4+} ions (Ce-1, Ce-2, Ce-3, and Ce-4), 6 Å apart from Cr; (E) structure in which three V_Os are introduced; two V_Os are located as neighbors of Cr and one is located far from Cr (6 Å) with all Ce^{3+} ions on NNN. Light green, sky blue, brown, dark blue, red, and gray balls represent the Ce^{4+} ion, Ce^{3+} ion, Cr^{4+} ion, Cr^{3+} ion, O, and V_O, respectively.

In the next place, the structural distortion effects induced by Cr doping are considered. Fig.6D shows the structure in which another oxygen atom moved away from the Cr ion after the formation of six-coordinated Cr^{3+} was removed. To simulate that, O-2 was removed from the structure shown in Fig.6C, maintaining the six-coordinated the Cr^{3+} with an even lower E_{V_O} of 0.65 eV. The V_O is located in the nearest neighbor (NN) position of Cr^{3+} ion, and three Ce^{3+} ions are located in the NNN of the V_O, as shown in Fig.6D. Further formation of V_O in Cr-substituted CeO_2 was calculated. Because of the large structural distortion due to the smaller ionic radius of Cr compared to Ce, Cr doping affects not only the neighboring oxygen atoms of Cr^{3+} but also other oxygen sites far from Cr^{3+}. For example, the E_{V_O} of O-3 in Fig.6D (6 Å from Cr) was 1.20 eV. A significantly lower E_{V_O} (1.20 eV) compared to the pristine CeO_2 (2.00 eV) was observed even at an O site away from Cr, i.e., O-3 was coordinated by four Ce^{4+} ions (Ce-1, Ce-2, Ce-3, and Ce-4 shown in Fig.6D) similar to the pristine CeO_2. Fig.6E shows the structure from which O-3 was removed, and all five compensating Ce^{3+} ions are located at the NNN of V_O. The low E_{V_O} of Cr-substituted CeO_2 NCs can lead to a significant increase in the fraction of Ce^{3+} ions even with 3 mol% Cr doping, as observed in the experiments.

A nudged elastic band calculation (NEB) was conducted to elucidate the mobility of oxygen for the pristine and Cr-substituted CeO_2. Fig.7A and B show the migration path of an oxygen atom to the vacancy site and migration barrier. Compared to pristine CeO_2 (0.41 eV), a much lower migration barrier was observed in the Cr-substituted CeO_2 (0.28 eV). Notably,

18

the migration barrier of oxygen in the Cr-substituted CeO_2 is much smaller than Cr_2O_3 (1.18 eV), according to a previous study.[62] In the pristine CeO_2, an electron polaron (Ce^{3+}) exists at the NNN of the V_O, and diffusion of the polaron accompanying the oxygen diffusion was observed; rapid polaron diffusion in reduced CeO_2 has been discussed previously [62]. As a result of the NEB calculation, the diffusion constants of the pristine CeO_2 and the Cr-substituted CeO_2 are 5×10^{-11} m^2 s^{-1} and 5×10^{-10} m^2 s^{-1} t 400 °C, respectively. Therefore, the increased oxygen mobility in the Cr-substituted CeO_2 is one of the origins of the high oxygen storage capacity observed in the experiments.
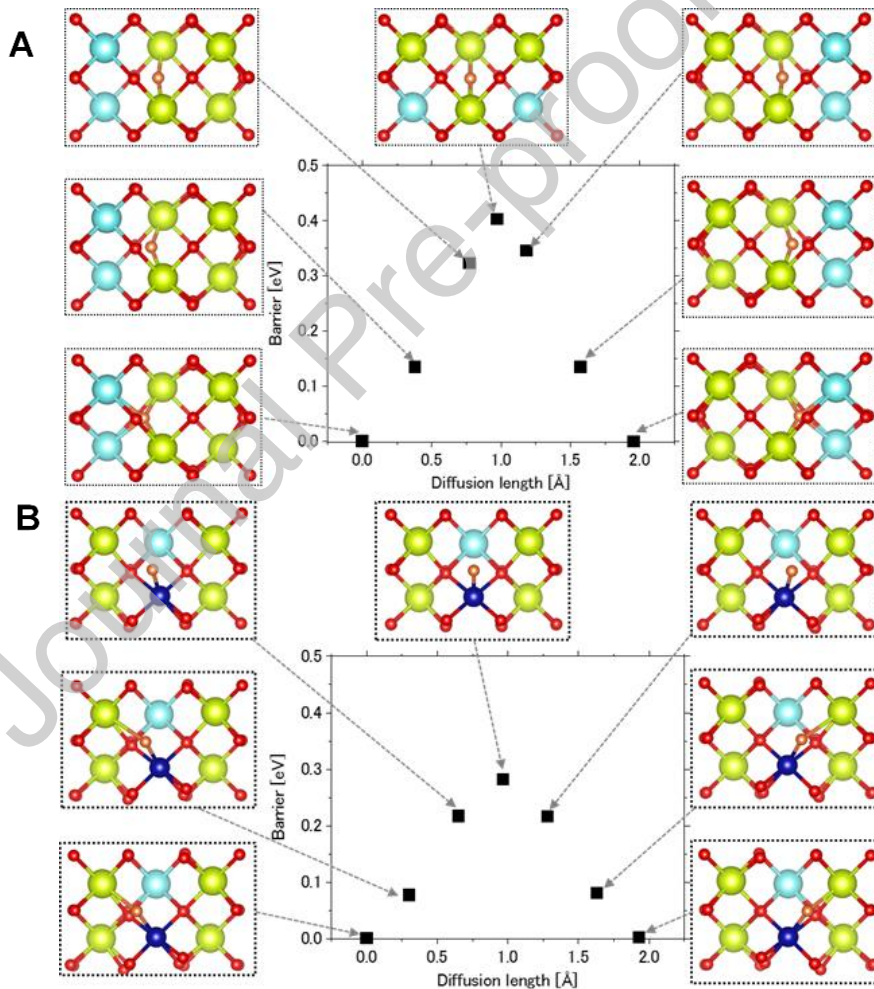
Fig.7. **Energy barrier of oxygen atom migration to a vacancy site** obtained from the NEB calculations for (A) the pristine CeO_2 and (B) the Cr-substituted CeO_2. Light green, sky blue,

19

dark blue, red, and orange balls represent Ce^{4+} ion, Ce^{3+} ion, Cr^{3+} ions, O, and diffusing oxygen, respectively.

4. Conclusions

In summary, to elucidate the effect of the dopant on the formation and distribution of Ce^{3+} cations inside the CeO_2 NCs, the Cr dopant was successfully introduced into the cubic {100}-faceted CeO_2 NCs with an average size of 7.8 nm. Combined with atomic-scale analysis using STEM-EELS and the theoretical calculations, the effect of Cr dopant on the distribution of Ce^{3+} cations and E_{V_O} have been thoroughly studied. The introduced Cr dopant substitutes Ce sites in a small loading amount of 3 mol%, and substantially decreases the E_{V_O} from 2.0 eV (the pristine CeO_2) to 0.99 eV, and further reduces it to 0.65 eV for the formation of an additional V_O. Local lattice distortion occurs around the Cr dopant, which in turn stabilizes the formed V_Os. Therefore, a considerably larger amount of the Ce^{3+} cation was detected in the Cr-substituted CeO_2 NCs, particularly in the internal atomic layers of the relatively larger NCs with the size over 7 nm, compared to the pristine CeO_2 NCs. Moreover, a high oxygen atoms mobility of 5×10^{-10} m^2 s^{-1} was observed for Cr-substituted CeO_2, which was approximately 10 times larger than the pristine CeO_2 at 400 °C. Therefore, the increase of V_Os with a high concentration and the high oxygen diffusivity improve the OSC performance of Cr-substituted CeO_2 NCs, compared with the pristine CeO_2 NCs. This quantitative analysis of the effect of the Cr dopant on the local structural distortion, the formation and distribution of V_O, provide valuable information for understanding the internal defective features inside the doped CeO_2, and may guide the fabrication and design of novel oxygen storage materials based on active dopants, nano-sizing and controllable exposed facets of the reduced CeO_2 NCs, which hold substantial promise in developing CeO_2-based nanocatalysts for use in the industrial applications.

20

Declaration of interests

☒ The authors declare that they have no known competing financial interests or personal relationships that could have appeared to influence the work reported in this paper.

Acknowledgements

References

[1]   Trovarelli, A., Catalytic properties of ceria and CeO_2-containing materials, Catal. Rev., 38 (1996) 439-520.

[2]   Kašpar, J., P. Fornasiero, and M. Graziani, Use of CeO_2-based oxides in the three-way catalysis, Catal. Today, 50 (1999) 285-298.

[3]   Graciani, J., K. Mudiyanselage, F. Xu, A.E. Baber, J. Evans, S.D. Senanayake, D.J. Stacchiola, P. Liu, J. Hrbek, and J.F. Sanz, Highly active copper-ceria and copper-ceria-titania catalysts for methanol synthesis from CO_2, Science, 345 (2014) 546-550.

[4]   Fu, X.P., L.W. Guo, W.W. Wang, C. Ma, C.J. Jia, K. Wu, R. Si, L.D. Sun, and C.H. Yan, Direct Identification of Active Surface Species for the Water-Gas Shift Reaction on a Gold-Ceria Catalyst, J. Am. Chem. Soc., 141 (2019) 4613-4623.

[5]   Lee, J.G., J.H. Park, and Y.G. Shul, Tailoring gadolinium-doped ceria-based solid oxide fuel cells to achieve 2 W cm^{-2} at 550 degrees C, Nat. Commun., 5 (2014) 4045.

[6]   Wang, B., B. Zhu, S. Yun, W. Zhang, C. Xia, M. Afzal, Y. Cai, Y. Liu, Y. Wang, and H. Wang, Fast ionic conduction in semiconductor $CeO_{2-\delta}$ electrolyte fuel cells, NPG Asia Mater., 11 (2019) 51.

[7]   Liu, X., K. Zhou, L. Wang, B. Wang, and Y. Li, Oxygen vacancy clusters promoting reducibility and activity of ceria nanorods, J. Am. Chem. Soc., 131 (2009) 3140-3141.

[8]   Chueh, W.C., C. Falter, M. Abbott, D. Scipio, P. Furler, S.M. Haile, and A. Steinfeld, High-flux solar-driven thermochemical dissociation of CO_2 and H_2O using nonstoichiometric ceria, Science, 330 (2010) 1797-1801.

[9]   Lawrence, N.J., J.R. Brewer, L. Wang, T.S. Wu, J. Wells-Kingsbury, M.M. Ihrig, G. Wang, Y.L. Soo, W.N. Mei, and C.L. Cheung, Defect engineering in cubic cerium oxide nanostructures for catalytic oxidation, Nano Lett., 11 (2011) 2666-2671.

[10]   Wang, D., Y. Kang, V. Doan-Nguyen, J. Chen, R. Kungas, N.L. Wieder, K. Bakhmutsky, R.J. Gorte, and C.B. Murray, Synthesis and oxygen storage capacity of two-dimensional ceria nanocrystals, Angew. Chem. Int. Ed., 50 (2011) 4378-4381.

[11]   Jiang, D., W. Wang, L. Zhang, Y. Zheng, and Z. Wang, Insights into the surface-defect dependence of photoreactivity over CeO_2 nanocrystals with well-fefined crystal facets, ACS Catal., 5 (2015) 4851-4858.

[12]   Ishikawa, Y., M. Takeda, S. Tsukimoto, K.S. Nakayama, and N. Asao, Cerium oxide nanorods with unprecedented low-temperature oxygen storage capacity, Adv. Mater., 28 (2016) 1467-71.

[13]   Zhang, J., S. Ohara, M. Umetsu, T. Naka, Y. Hatakeyama, and T. Adschiri, Colloidal ceria nanocrystals: A tailor-made crystal morphology in supercritical water, Adv. Mater., 19 (2007) 203-206.

[14]   Zhang, J., H. Kumagai, K. Yamamura, S. Ohara, S. Takami, A. Morikawa, H. Shinjoh, K. Kaneko, T. Adschiri, and A. Suda, Extra-low-temperature oxygen storage capacity of CeO_2 nanocrystals with cubic facets, Nano Lett., 11 (2011) 361-364.

[15]   Litwinowicz, A.A., S. Takami, S. Asahina, X. Hao, A. Yoko, G. Seong, T. Tomai, and T. Adschiri, Formation dynamics of mesocrystals composed of organically modified CeO_2 nanoparticles: analogy to a particle formation model, CrystEngComm, 21 (2019) 3836-3843.

[16]   Hao, X., C. Chen, M. Saito, D. Yin, K. Inoue, S. Takami, T. Adschiri, and Y. Ikuhara, Direct imaging for single molecular chain of surfactant on CeO_2 nanocrystals, Small, 14 (2018) 1801093.

[17]   Hao, X., A. Yoko, C. Chen, K. Inoue, M. Saito, G. Seong, S. Takami, T. Adschiri, and Y. Ikuhara, Atomic scale valence state distribution inside ultrafine CeO_2 nanocubes and its size dependence, Small, 14 (2018) 1802915.

[18]   Aneggi, E., D. Wiater, C. de Leitenburg, J. Llorca, and A. Trovarelli, Shape-Dependent Activity of Ceria in Soot Combustion, ACS Catal., 4 (2013) 172-181.

22

[19] Mai, H.X., L.D. Sun, Y.W. Zhang, R. Si, W. Feng, H.P. Zhang, H.C. Liu, and C.H. Yan, Shape-selective synthesis and oxygen storage behavior of ceria nanopolyhedra, nanorods, and nanocubes, J. Phys. Chem. B, 109 (2005) 24380-24385.

[20] Trovarelli, A. and J. Llorca, Ceria Catalysts at Nanoscale: How Do Crystal Shapes Shape Catalysis?, ACS Catal., 7 (2017) 4716-4735.

[21] Mamontov, E., T. Egami, R. Brezny, M. Koranne, and S. Tyagi, Lattice defects and oxygen storage capacity of nanocrystalline ceria and ceria-zirconia, J. Phys. Chem. B, 104 (2000) 11110-11116.

[22] Liu, X., J. Ding, X. Lin, R. Gao, Z. Li, and W. Dai, Zr-doped CeO_2 nanorods as versatile catalyst in the epoxidation of styrene with tert-butyl hydroperoxide as the oxidant, Appl. Catal., A, 503 (2015) 117-123.

[23] Feng, X., D.C. Sayle, Z.L. Wang, M.S. Paras, B. Santora, A.C. Sutorik, T.X. Sayle, Y. Yang, Y. Ding, and X. Wang, Converting ceria polyhedral nanoparticles into single-crystal nanospheres, Science, 312 (2006) 1504-1508.

[24] Gupta, A., U.V. Waghmare, and M.S. Hegde, Correlation of Oxygen Storage Capacity and Structural Distortion in Transition-Metal-, Noble-Metal-, and Rare-Earth-Ion-Substituted CeO_2 from First Principles Calculation, Chem. Mater., 22 (2010) 5184-5198.

[25] Yao, X., C. Tang, Z. Ji, Y. Dai, Y. Cao, F. Gao, L. Dong, and Y. Chen, Investigation of the physicochemical properties and catalytic activities of $Ce_{0.67}M_{0.33}O_2$($M = Zr^{4+}$, Ti^{4+}, Sn^{4+}) solid solutions for NO removal by CO, Catal. Sci. Technol., 3 (2013) 688-698.

[26] Slostowski, C., S. Marre, J.-M. Bassat, and C. Aymonier, Synthesis of cerium oxide-based nanostructures in near-and supercritical fluids, J. Supercrit. Fluid., 84 (2013) 89-97.

[27] Elias, J.S., M. Risch, L. Giordano, A.N. Mansour, and Y. Shao-Horn, Structure, bonding, and catalytic activity of monodisperse, transition-metal-substituted CeO_2 nanoparticles, J. Am. Chem. Soc., 136 (2014) 17193-17200.

[28] Yu, W.Z., W.W. Wang, S.Q. Li, X.P. Fu, X. Wang, K. Wu, R. Si, C. Ma, C.J. Jia, and C.H. Yan, Construction of Active Site in a Sintered Copper–Ceria Nanorod Catalyst, J. Am. Chem. Soc., 141 (2019) 17548-17557.

[29] Harrington, G.F., L. Sun, B. Yildiz, K. Sasaki, N.H. Perry, and H.L. Tuller, The interplay and impact of strain and defect association on the conductivity of rare-earth substituted ceria, Acta Mater., 166 (2019) 447-458.

[30] Auxéméry, A., B.B. Frias, E. Smal, K. Dziadek, G. Philippot, P. Legutko, M. Simonov, S. Thomas, A. Adamski, and V. Sadykov, Continuous supercritical solvothermal preparation of nanostructured ceria-zirconia as supports for dry methane reforming catalysts, J. Supercrit. Fluid., 162 (2020) 104855.

[31] Sugiura, M., Oxygen storage materials for automotive catalysts: ceria-zirconia solid solutions, Catal. Surv. Asia, 7 (2003) 77-87.

[32] Di Monte, R. and J. Kašpar, On the role of oxygen storage in three-way catalysis, Top. Catal., 28 (2004) 47-57.

[33] Song, S.H., J. Moon, J.H. Kim, J. Hong, J.-H. Lee, H.-W. Lee, B.-K. Kim, and H. Kim, Panoscopic alloying of cobalt in CeO_2–ZrO_2 solid solutions for superior oxygen-storage capacity, Acta Mater., 113 (2016) 206-212.

[34] Ozawa, M., M. Misaki, M. Iwakawa, M. Hattori, K. Kobayashi, K. Higuchi, and S. Arai, Low content Pt-doped CeO_2 and core-shell type CeO_2/ZrO_2 model catalysts; microstructure, TPR and three way catalytic activities, Catal. Today, 332 (2019) 251-258.

[35] McFarland, E.W. and H. Metiu, Catalysis by Doped Oxides, Chem. Rev., 113 (2013) 4391-4427.

[36] Singh, P., M. Hegde, and J. Gopalakrishnan, $Ce_{2/3}Cr_{1/3}O_{2+y}$: a new oxygen storage material based on the fluorite structure, Chem. Mater., 20 (2008) 7268-7273.

[37] Singh, P. and M. Hegde, $Ce_{0.67}Cr_{0.33}O_{2.11}$: A new low-temperature O_2 evolution material and H_2 generation catalyst by thermochemical splitting of water, Chem. Mater., 22 (2009) 762-768.

[38] Zhu, Y., G. Seong, T. Noguchi, A. Yoko, T. Tomai, S. Takami, and T. Adschiri, Highly Cr-Substituted CeO_2 Nanoparticles Synthesized Using a Non-equilibrium Supercritical Hydrothermal Process: High Oxygen Storage Capacity Materials Designed for a Low-Temperature Bitumen Upgrading Process, ACS Appl. Energy Mater., 3 (2020) 4305-4319.

[39] Xie, H., H. Wang, Q. Geng, Z. Xing, W. Wang, J. Chen, L. Ji, L. Chang, Z. Wang, and J. Mao, Oxygen Vacancies of Cr-Doped CeO_2 Nanorods That Efficiently Enhance the Performance of Electrocatalytic N_2 Fixation to NH_3 under Ambient Conditions, Inorg. Chem., 58 (2019) 5423-5427.

[40] Wang, Y., X. Bai, F. Wang, S. Kang, C. Yin, and X. Li, Nanocasting synthesis of chromium doped mesoporous CeO_2 with enhanced visible-light photocatalytic CO_2 reduction performance, Journal of Hazardous Materials, 372 (2019) 69-76.

[41] Li, X., S. Wei, Z. Zhang, Y. Zhang, Z. Wang, Q. Su, and X. Gao, Quantification of the active site density and turnover frequency for soot combustion with O_2 on Cr doped CeO_2, Catal. Today, 175 (2011) 112-116.

[42] Izumi, F. and K. Momma. *Three-dimensional visualization in powder diffraction*. in *Solid State Phenomena*. 2007. Trans Tech Publ.

[43] Kresse, G. and J. Furthmüller, Efficient iterative schemes for ab initio total-energy calculations using a plane-wave basis set, Phys. Rev. B, 54 (1996) 11169.

[44] Kresse, G. and D. Joubert, From ultrasoft pseudopotentials to the projector augmented-wave method, Phys. Rev. B, 59 (1999) 1758.

[45] Perdew, J.P., K. Burke, and M. Ernzerhof, Generalized gradient approximation made simple, Phys. Rev. Lett., 77 (1996) 3865.

[46] Dudarev, S., G. Botton, S. Savrasov, C. Humphreys, and A. Sutton, Electron-energy-loss spectra and the structural stability of nickel oxide: An LSDA+ U study, Phys. Rev. B, 57 (1998) 1505.

[47] Shannon, R.D., Revised effective ionic radii and systematic studies of interatomic distances in halides and chalcogenides, Acta Crystallogr., Sect. A: Cryst. Phys., Diffr., Theor. Gen. Crystallogr., 32 (1976) 751-767.

[48] Keating, P.R., D.O. Scanlon, B.J. Morgan, N.M. Galea, and G.W. Watson, Analysis of intrinsic defects in CeO_2 using a Koopmans-like GGA+ U approach, J. Phys. Chem. C, 116 (2012) 2443-2452.

[49] Murnaghan, F., The compressibility of media under extreme pressures, Proc. Natl. Acad. Sci. U. S. A., 30 (1944) 244-247.

[50] Birch, F., Finite Elastic Strain of Cubic Crystals, Phys. Rev., 71 (1947) 809-824.

[51] Momma, K. and F. Izumi, VESTA 3 for three-dimensional visualization of crystal, volumetric and morphology data, J. Appl. Crystallogr., 44 (2011) 1272-1276.

[52] Henkelman, G., B.P. Uberuaga, and H. Jónsson, A climbing image nudged elastic band method for finding saddle points and minimum energy paths, J. Chem. Phys., 113 (2000) 9901-9904.

[53] Yoko, A., N. Umezawa, T. Ohno, and Y. Oshima, Impact of surface energy on the formation of composite metal oxide nanoparticles, J. Phys. Chem. C, 122 (2018) 24350-24358.

[54] Daulton, T.L. and B.J. Little, Determination of chromium valence over the range Cr(0)–Cr(VI) by electron energy loss spectroscopy, Ultramicroscopy, 106 (2006) 561-573.

[55]   Fortner, J.A. and E.C. Buck, The chemistry of the light rare-earth elements as determined by electron energy loss spectroscopy, Appl. Phys. Lett., 68 (1996) 3817-3819.

[56]   Dejhosseini, M., T. Aida, M. Watanabe, S. Takami, D. Hojo, N. Aoki, T. Arita, A. Kishita, and T. Adschiri, Catalytic cracking reaction of heavy oil in the presence of cerium oxide nanoparticles in supercritical water, Energ. Fuel., 27 (2013) 4624-4631.

[57]   Ganduglia-Pirovano, M.V., J.L. Da Silva, and J. Sauer, Density-functional calculations of the structure of near-surface oxygen vacancies and electron localization on CeO_2 (111), Phys. Rev. Lett., 102 (2009) 026101.

[58]   Alla, S.K., E.V. Prasadarao Komarala, R.K. Mandal, and N.K. Prasad, Structural, optical and magnetic properties of Cr-substituted CeO_2 nanoparticles, Mater. Chem. Phys., 182 (2016) 280-286.

[59]   Yu, M. and D.R. Trinkle, Accurate and efficient algorithm for Bader charge integration, J. Chem. Phys., 134 (2011) 064111.

[60]   Gray, C., Y. Lei, and G. Wang, Charged vacancy diffusion in chromium oxide crystal: DFT and DFT+ U predictions, J. Appl. Phys., 120 (2016) 215101.

[61]   Wang, B., X. Xi, and A.N. Cormack, Chemical strain and point defect configurations in reduced ceria, Chem. Mater., 26 (2014) 3687-3692.

[62]   Nakayama, M., H. Ohshima, M. Nogami, and M. Martin, A concerted migration mechanism of mixed oxide ion and electron conduction in reduced ceria studied by first-principles density functional theory, Phys. Chem. Chem. Phys., 14 (2012) 6079-6084.

Graphical Abstract